

Developing an Insect Odorant Receptor Bioelectronic Nose  
for Vapour-Phase Sensing

by

Eddyn Oswald Perkins Treacher

A thesis submitted in fulfilment of the  
requirements of the degree of  
Doctor of Philosophy in Physics  
School of Physical and Chemical Sciences  
Te Herenga Waka - Victoria University of Wellington

May 2024





# Abstract

This is a thesis skeleton written with quarto. Make a copy of this thesis repo and start to write!

Make a new paragraph by leaving a blank line.



# Acknowledgements

B3 partnership!

At the university

Rifat, Alex - vapour sensor design and construction Peter Coard - electronics work Erica Cassie - FET sensing setup Rob Keyzers and Jennie Ramirez-Garcia - NMR spectra Patricia Hunt - Computational chemistry Erica Happe - steaming method Danica- AFM imaging Sushila Pillai - Fluorescence microscope training Jenna and Ali - Device functionalisation

Interns Lotte Boer Liam Anderson Hayden Young

Nick Grinter - vapour sensor setup Grant Franklin - vapour sensor setup Alan Rennie and Alex Puglisi - vapour sensor setup

Family and friends

Oldest friends - Bennett, Jaquille High school friends Undergrad friends Friends on Discord Je - gym Aikido group (Ian, Lee, Jak, Tim) Extended whanau Mum and Dad Nina!



# Table of Contents

<b>Abstract</b>	<b>i</b>
<b>Acknowledgements</b>	<b>iii</b>
<b>Table of Contents</b>	<b>v</b>
<b>List of Figures</b>	<b>vii</b>
<b>List of Tables</b>	<b>ix</b>
<b>List of Abbreviations</b>	<b>xi</b>
<b>1. Introduction</b>	<b>1</b>
<b>2. Vapour Sensing System for Transistor Biosensing</b>	<b>3</b>
2.1. General Overview . . . . .	3
2.2. Technical Notes . . . . .	4
2.2.1. Delivery System . . . . .	4
2.2.2. Reference Sensors . . . . .	4
2.2.3. Control System . . . . .	7
2.3. Design . . . . .	10
2.3.1. Initial Design . . . . .	10
2.3.2. Stage I Design . . . . .	10
2.3.3. Stage II Design . . . . .	12
2.4. Calibration and Measurements of Vapour Flow . . . . .	14
2.4.1. Chamber Flow Calibration . . . . .	14
2.4.2. Sensor Responses to Vapour Flow . . . . .	16
2.5. Summary . . . . .	22
<b>References</b>	<b>23</b>
<b>Appendices</b>	<b>25</b>
<b>A. Vapour System Hardware</b>	<b>25</b>
<b>B. Python Code for Data Analysis</b>	<b>27</b>
B.1. Code Repository . . . . .	27

*Table of Contents*

B.2. Atomic Force Microscope Histogram Analysis . . . . .	27
B.3. Raman Spectroscopy Analysis . . . . .	27
B.4. Field-Effect Transistor Analysis . . . . .	27

# List of Figures

2.1. The three mass flow controllers (MFCs) of the vapour delivery system are shown in (a), each with a regulator to set the pressure at the MFC inlet. (1) is the 20 sccm full-scale flow MFC, (2) is the 200 sccm full-scale flow MFC, and (3) is the 500 sccm full-scale flow MFC. The device chamber, reference sensors and other chamber peripherals are shown in (b). The components are labelled as follows: (1) Device chamber, (2) Photoionisation detector (PID), (3) Flowmeter from chamber to PID, (4) Micropump from chamber to PID, (5) Relative humidity and temperature monitor. . . . .	5
2.2. Images of the vapour delivery control system circuit board, where (a) shows the low-flow configuration and (b) shows the high-flow configuration. Components are labelled as follows: (1) 9-pin carrier line port, (2) 9-pin dilution line port, (3) red dilution port switch (determines which dilution line port is active), (4) 25-pin dilution line port. . . . .	8
2.3. Circuit board schematic for controlling and monitoring both the mass flow controllers and the relative humidity and temperature sensor. Resistors R1-R6 are all 10 kOhm, while R7-R8 are both 0 Ohm. The circuit board was designed using the KiCad Layout Editor. . . . .	9
2.4. P&ID of the original vapour delivery system . . . . .	10
2.5. P&ID of the Stage I vapour delivery system. . . . .	11
2.6. Process & instrumentation diagram (P&ID) of the second-stage design for the vapour delivery system. Red outlines indicate additions introduced to the system subsequent to the first stage design. . . . .	13
2.7. Setup for calibration of mass flow controllers using the water displacement method. . . . .	14
2.8. The nominal flow rate as measured by the mass flow controller compared to the actual flow rate measured using water displacement testing, shown for the 200 sccm full-scale mas flow controller placed through the carrier line in (a), and for the 500 sccm full-scale mass flow controller placed through the dilution line in (b). Three water displacement tests were performed for each constant flow rate. . . . .	15
2.9. Comparison of flowmeter readings with flow measurements from water displacement testing. Three water displacement tests were performed for each constant flow rate. . . . .	16

*List of Figures*

2.10. Simplified schematic showing the flow into and out of the device chamber and manifold of the delivery system. The input flows from the carrier and dilution line are represented by C and D, and the output flow through the PID is represented by P. The exhaust can either flow past the relative humidity indicator or straight to the fumehood. This diagram assumes that flow through leaks in the chamber and manifold is low enough to be considered negligible, which was confirmed by leak testing with bubble solution. . . . .	17
2.11. Relative humidity readouts from the relative humidity indicator juxtaposed with flow rates from the dilution line and carrier lines of the vapour system, with 10 mL deionised water in the carrier line analyte bottle. . . . .	18
2.12. The response of the photoionisation detector to ethyl hexanoate vapour over 600 s of exposure is shown relative to the 200 sccm nitrogen flow baseline in (a), and normalised with respect to the maximum reading in (b). . . . .	20
2.13. The response of the photoionisation detector to 3 evenly-spaced intervals of ethyl hexanoate vapour entering the device chamber, relative to a 200 sccm nitrogen flow baseline. Input intervals were either either 50 s, 100 s or 200 s in length. During each input interval, 150 sccm carrier flow and 50 sccm dilution flow was placed through the chamber. . . . .	21

# List of Tables

2.1. Flow sequence for testing relative humidity indicator. . . . .	17
A.1. Major components used in construction of the vapour delivery system described in this thesis. . . . .	25



# List of Abbreviations

Ab	Antibody
AB	Amyl Butyrate
AFM	Atomic Force Microscope/Microscopy
AH	Absolute Humidity
Avi-tag	Avidin-tag
BMIM	1-Butyl-3-methylimidazolium bis(trifluoromethylsulfonyl)imide
CAD	Computer Aided Design
CNT	Carbon Nanotube
CVD	Chemical Vapour Deposition
DAN	1,5-diaminonaphthalene
DAQ	Data Acquisition Input/Output Module
DCB	1,2-dichlorobenzene
DI	Deionised
DMT-MM	4-(4,6-dimethoxy-1,3,5-triazin-2-yl)-4 methylmorpholinium chloride
DMMP	Dimethyl Methylphosphonate
DNA	Deoxyribonucleic Acid
EB	Ethyl Butyrate
EDL	Electric Double Layer
FET	Field-Effect Transistor
FITC	Fluorescein isothiocyanate
GA	Glutaraldehyde
GFET	Graphene Field-Effect Transistor
GFP	Green Fluorescent Protein
GPCR	G-protein Coupled Receptor
HEK	Human Embryonic Kidney
His-tag	Histidine-tag
hOR	Human Odorant Receptor
HPLC	High-performance Liquid Chromatography
iOR	Insect Odorant Receptor
IPA	Isopropanol
LOD	Limit of Detection
m-CNT	Metallic Carbon Nanotube

MFC	Mass Flow Controller
mOR	Mouse Odorant Receptor
MOSFET	Metal-Oxide-Semiconductor Field-Effect Transistor
MSP	Membrane Scaffold Protein
MWCNT	Multi-Walled Carbon Nanotube
NSB	Non-Specific Binding
NTA	Nitrilotriacetic Acid
OBP	Odorant Binding Protein
OR	Odorant Receptor
ORCO	Odorant Receptor Co-Receptor
PBASE	1-Pyrenebutanoic Acid N-hydroxysuccinimide Ester
PBS	Phosphate-Buffered Saline
PCB	Printed Circuit Board
PDL	Poly- <i>D</i> -lysine
PDMS	Polydimethylsiloxane
PEG	Polyethylene Glycol
PID	Photoionisation Detector
PLL	Poly- <i>L</i> -lysine
PTFE	Polytetrafluoroethylene (Teflon <sup>TM</sup> )
PVC	Polyvinyl chloride
RH	Relative Humidity
RHI	Relative Humidity and Temperature Indicator
RNA	Ribonucleic Acid
s-CNT	Semiconducting Carbon Nanotube
SEM	Scanning Electron Microscope
SMU	Source Measure Unit
SWCNT	Single-Walled Carbon Nanotube
TFTFET	Thin-Film Field-Effect Transistor
TMAH	Tetramethylammonium hydroxide
TX	Transfer Characteristics
UV	Ultraviolet
VI	Virtual Instrument
VUAA1	N-(4-Ethylphenyl)-2-[4-ethyl-5-(pyridin-3-yl)-4H-1,2,4-triazol-3-yl]sulfanylacetamide





# 1. Introduction

My aim is to develop a ‘bioelectronic nose’, a biosensor device which couples sensitive biological recognition elements with an electronic transducer for the detection of vapour phase compounds [1]–[3]. The transducer converts the interaction or interactions between the recognition element and analyte or analytes of interest into a measurable electronic signal. The sensitive biological component used here are *Drosophila melanogaster* insect odorant receptors (iORs), while the electronic transducer element is a carbon nanotube- or graphene-based field effect transistor (CNTFET or GFET). Carbon-based 2D nanomaterials are promising for use in novel biosensors as they are highly sensitive, biocompatible and cheap to fabricate [4]. I created a purpose-built vapour delivery system apparatus in order to test these devices. Initially, however, iOR-functionalised CNTFETs and GFETs (iOR-FETs) were first tested in the liquid phase to corroborate previous findings within my research group [5], [6].

There has been a significant amount of work done towards creating bioelectronic noses over the last twenty years. This is largely due to their promisingly high level of sensitivity and specificity in real-time in the gas phase, with the ability to signal the presence of volatile organic compound (VOC) traces at lower concentrations than traditional chemical sensors or the human nose in a timescale of seconds [1], [3], [7]. The implications of successful development of a portable and robust bioelectronic nose are significant and varied. Applications could be found in high-importance fields such as biosecurity, medicine, environmental protection and food or water safety [2], [8]–[10]. It has been demonstrated that it is possible to detect invasive brown marmorated stinkbugs based on their volatile trace [11]. A bioelectronic nose could potentially accomplish this task far more cheaply and efficiently than trained sniffer dogs.

As well as a variety of practical applications, development of a bioelectronic nose may give us a greater understanding of the mechanisms underlying insect olfaction, as well as novel understandings of the transducer devices used to register the electronic response to VOCs [1]. The transduction mechanism of nanomaterial-based iOR sensors is still unknown, and I hope to shed further light on the biological and electronic processes underpinning this mechanism [6], [12].



## 2. Vapour Sensing System for Transistor Biosensing

### 2.1. General Overview

Through the adaptation of an existing setup, a custom vapour delivery system was developed to measure the response of field-effect biosensors to vapour. To achieve this goal, the new system needed to meet three requirements:

- The ability to automatically deliver a vapour to an enclosed environment in a controlled manner.
- The ability to collect measurements from a sensor device within that environment.
- The ability to collect data from off-the-shelf reference sensors monitoring the same environment, for comparison with data collected by the novel biosensor.

The existing system had a limited ability to meet the first two requirements, but was not able to take reference measurements of vapour flow. To implement new elements that would enable the system to fulfill all three requirements, a two-step development approach was taken across the course of the thesis. The changes made with each step of the redesign are outlined in Section 2.3.

Three mass flow controllers (MFC) were used to precisely control and monitor the flow of nitrogen into the system in units of standard cubic centimeters per minute (sccm). The manner in which these controllers were configured in the system is discussed in Section 2.2.1. The reference sensors chosen were a photoionisation detector (Ametek Mocon) and relative humidity and temperature indicator (Telaire). The photoionisation detector is able to monitor a wide range of volatile organic compounds, but cannot monitor compounds with an ionisation energy exceeding 10.6 eV. This includes nitrogen, oxygen, carbon dioxide, argon and water [13], [14]. Therefore, the photoionisation detector (PID) should not respond to either ambient air or standard nitrogen flow through the detector. As we would also like to monitor the presence of water vapour in the system, we use a relative humidity and temperature indicator (RHI). The operation of these reference sensors is discussed further in Section 2.2.2.

## 2.2. Technical Notes

### 2.2.1. Delivery System

Three mass flow controllers (MFCs) and their associated regulators sit in a covered enclosure, seen from the front in Figure 2.1 (a). The MFCs are used to control the nitrogen flow rate through two delivery lines, the carrier line and dilution line. Each line consists of a mix of stainless steel and flexible PVC tubing, with various Swagelok fittings and valves; these valves include check valves, to ensure there is no vapour backflow. The system is designed so that only one MFC delivers flow through each line. Furthermore, the mass flow controller with a full-scale flow of 500 sccm (standard cubic centimeters per minute) can only be directed through the dilution line, and the mass flow controller with a full-scale flow of 20 sccm can only be directed through the carrier line. The dilution and carrier lines merge at a mixing point about a metre before the device chamber, which contains the device being tested. Flow through the carrier line is bubbled through a volatile compound within a sealed 10 mL Schott bottle (Duran). A three-way valve determines whether the analyte vapour is then carried towards the mixing point or sent to the system exhaust.

### 2.2.2. Reference Sensors

Two reference sensors were added to the vapour delivery setup to compare the response to vapour by the fabricated sensor device with some reference signal. These reference sensors are a photoionisation detector (Ametek Mocon) and a relative humidity and temperature indicator (Telaire). The layout of these reference sensors (and their associated peripherals) relative to the device chamber is shown in Figure 2.1 (b). These components are on a raised platform directly above the mass flow controller enclosure. Vapour flowing through the device chamber passes into a cylindrical manifold with three outlets. One outlet is the system exhaust, one flows into relative humidity indicator chamber, and one flows into the photoionisation detector. A dial-controlled micro diaphragm pump is used to set the flow rate from the manifold into the photoionisation detector, with a flowmeter used to monitor this flow rate. The electronic integration and programming of the relative humidity and temperature indicator is described in Section 2.2.3. The photoionisation detector was connected to a laptop directly via USB, then controlled and monitored using the supplier-provided VOC-TRAQ II software package.

#### Relative Humidity and Temperature Indicator

The relative humidity and temperature indicator used here is a capacitive humidity sensor [15]. It consists of a capacitor with a hygroscopic polymer as the capacitor dielectric. As room temperature water has a much larger dielectric constant than the

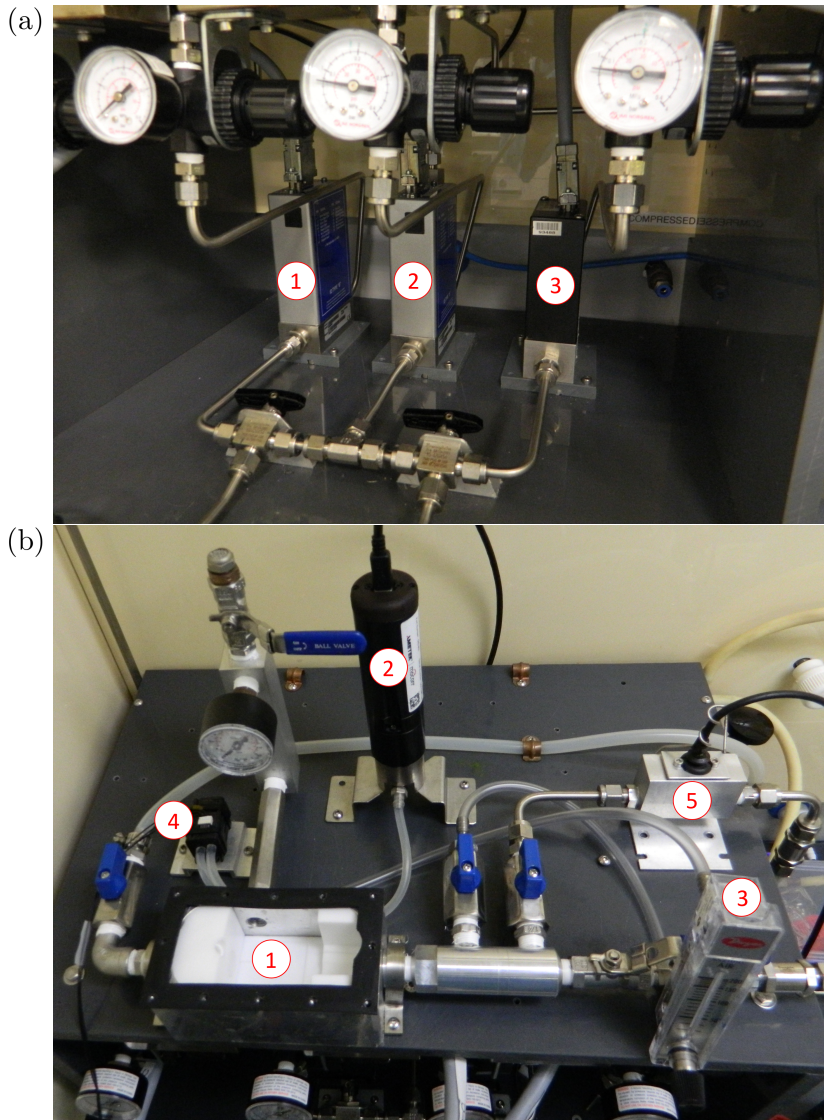


Figure 2.1.: The three mass flow controllers (MFCs) of the vapour delivery system are shown in (a), each with a regulator to set the pressure at the MFC inlet. (1) is the 20 sccm full-scale flow MFC, (2) is the 200 sccm full-scale flow MFC, and (3) is the 500 sccm full-scale flow MFC. The device chamber, reference sensors and other chamber peripherals are shown in (b). The components are labelled as follows: (1) Device chamber, (2) Photoionisation detector (PID), (3) Flowmeter from chamber to PID, (4) Micropump from chamber to PID, (5) Relative humidity and temperature monitor.

polymer dielectric, absorption of water by the polymer leads to increased sensor capacitance [16]. The sensor capacitance, corresponding to the amount of moisture absorbed by the polymer and therefore the relative humidity, is then translated by the sensor into a calibrated electronic output. This output is then processed using the hardware and software described in Section 2.2.3 to give a value for the relative humidity. The sensor has a quoted relative humidity (RH) accuracy of  $\pm 2.0\%$  when RH is below 80%, and has a quoted temperature accuracy of  $0.5^\circ\text{C}$  [15]. The absolute humidity (AH), the mass of water vapour within a set volume, can be calculated in  $\text{gm}^{-3}$  using Equation 2.1.

$$AH = C \frac{P_W}{T} \quad (2.1)$$

Here,  $C = 2.16679 \text{ gKJ}^{-1}$ ,  $P_W$  is the water vapour pressure (in Pa) and T is the temperature (in K) [17]. For temperatures between  $-20^\circ\text{C}$  and  $50^\circ\text{C}$ , water vapour pressure  $P_W$  (in hPa) can be approximated using Equation 2.2.

$$P_W = RH \times A \times 10^{(mT/(T+T_n))} \quad (2.2)$$

Here, RH is relative humidity, T is temperature in  $^\circ\text{C}$ ,  $A = 6.116441 \text{ hPa}$ ,  $m = 7.591386$  and  $T_n = 240.7263^\circ\text{C}$  [17].

### Photoionisation Detector

A photoionisation detector (PID) can be used to continuously monitor volatile organic compounds by measuring the extent to which vapour molecules passing through the detector can be ionised. A small percentage of vapour molecules flowing into the detector diffuse into a sensor cavity. This cavity is bounded on each side by a pair of electrodes. A lamp in the body of the detector radiates UV light through a window into this cavity. The vapour molecules have their outer-most electrons excited and removed when struck with these high-energy photons. The ionised molecules then drift towards the sensor cathode, while free electrons drift towards the sensor anode. This results in a current proportional to the concentration of vapour molecules in the chamber. The current can then be amplified for a signal readout. To be detected, the ionisation energy of the molecules being monitored cannot exceed the energy of the incident UV light. Therefore, molecules of clean air will not be detected. Likewise, volatile organic compounds with high ionisation energy — such as methane — will not be recognised by the PID. Conversely, if the energy required to ionise a volatile of interest is relatively low, the PID will generally show a relatively large response to that volatile [13], [14].

The photoionisation detector lamps used in this work each had a lamp energy of 10.6 eV, with a quoted response time of less than 2 seconds. Photoionisation detectors are designed to sensitively detect within a particular concentration range. PID sensors can become less sensitive after being exposed to very high concentrations of volatile gas. They can also become less sensitive if exposed to high levels of humidity or volatile

substances known to contaminate the PID window, which are not used in this thesis. The typical sensitivity range of a PID can be stated in terms of the sensor response to isobutylene gas, which is typically used to calibrate PID sensors. The sensitivity ranges of the two PID sensors used here were 10 ppb – 200 ppm and 100 ppb – 2,000 ppm. Calibration with a reference gas ensures the detector reads the true concentration of volatiles being detected, multiplied by some previously-documented factor called a “response factor”. However, these response factors can vary based on the design of the PID and various environmental factors [13], [14].

In this work, the PID was operated without end-user calibration. PID measurements were used to confirm the evolution of vapour presence in the chamber over time. It should be expected that sensor sensitivity will exhibit span drift over days or weeks, depending on changes in the local environment, and therefore measurements should not be treated as absolute measurements that correspond to a true concentration reading. A sampling rate of 1 s was used for all measurements. When sampling vapour concentration, baseline measurements of nitrogen flow through the PID were used as the zero concentration reference point. The vapour of interest can be delivered to the PID either through diffusion or by means of a low-power pump. A micro diaphragm pump (Xavitech) was selected to pump the vapour from the chamber into the PID detector. A pump with a low maximum flow rate was selected since the PID requires an inlet flow of less than 300 sccm. As the pump is controlled using an unlabelled dial, a flowmeter was used to independently measure the flow rate through the micropump into the PID.

### 2.2.3. Control System

The vapour delivery system was controlled and monitored from a laptop connected to a National Instruments USB-6009 multifunction data acquisition input/output module (DAQ). This USB-6009 DAQ connected to the mass flow controllers and relative humidity and temperature indicator (Telaire) via a custom-designed circuit board manufactured by PCBway. The outputs and inputs of the USB-6009 DAQ were set using custom LabView software. These electronic and software components of the vapour delivery control system are described in more detail below. The photoionisation detector (Ametek Mocon) was controlled from the same laptop with its own prepackaged software (VOC-TRAQ II).

### Electronics

Figure 2.2 shows the control circuit board required to connect the mass flow controllers and relative humidity indicator to the NI USB-6009. Only one mass flow controller can be set to provide flow to a specific line. Therefore, only two mass flow controllers can be operational simultaneously during testing. The control circuit board allows the user to select the two mass flow controllers to be used during a specific test run. Figure 2.2 (a) shows the ‘high-flow’ configuration, where the 500 sccm full-scale MFC is connected

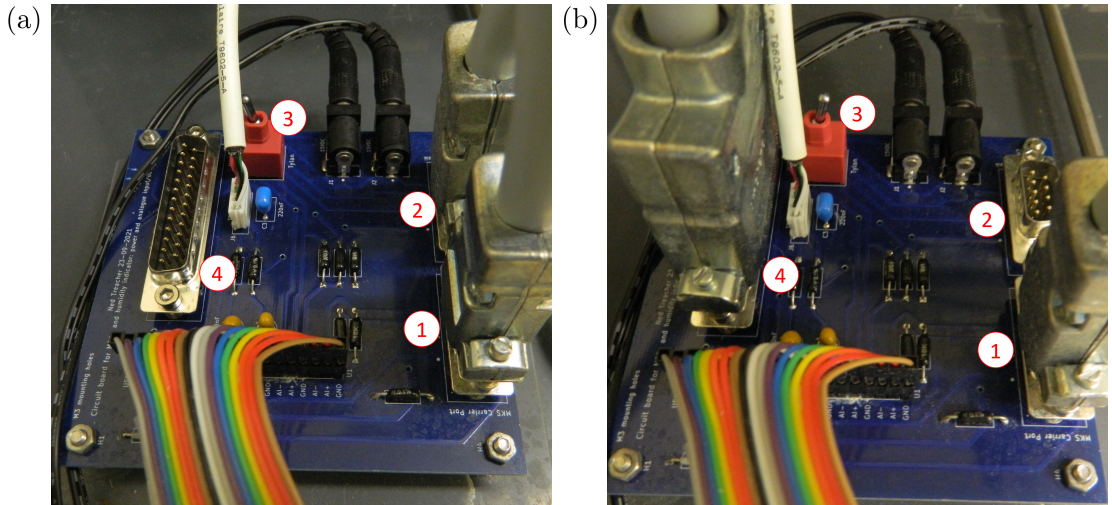


Figure 2.2.: Images of the vapour delivery control system circuit board, where (a) shows the low-flow configuration and (b) shows the high-flow configuration. Components are labelled as follows: (1) 9-pin carrier line port, (2) 9-pin dilution line port, (3) red dilution port switch (determines which dilution line port is active), (4) 25-pin dilution line port.

at the 25-pin dilution line port, the 200 sccm full-scale MFC is connected to the 9-pin carrier line port, and red dilution port switch is towards ‘Tylan’ (rightwards). Figure 2.2 (b) shows the ‘low-flow’ configuration, where the 200 sccm full-scale MFC is connected to the 9-pin dilution line port, the 20 sccm full-scale MFC is connected to the 9-pin carrier line port and the red dilution port switch is towards ‘MKS’ (leftwards). The design for the circuit board is shown in Figure 2.3, showing the USB-6009 pinout. The relative humidity and temperature sensor is connected to the circuit board via the T9602 footprint. In the ‘high-flow’ configuration, the Tylan dilution and MKS carrier ports are connected to the corresponding MFCs, with switch SW1 is towards ‘Tylan’. In the ‘low-flow’ configuration, both MKS ports are connected, and switch SW1 is towards ‘MKS’.

## Software

Two LabView Virtual Instruments (VIs) were adapted from pre-existing VIs for operating the mass flow controllers and monitoring vapour flow into the device chamber, as well as monitoring temperature and humidity in the vapour delivery system’s manifold. These VIs were named ‘vapour-sensor-basic.vi’ and ‘temp-and-humidity-basic.vi’. A third VI was developed in parallel which combined the first two Virtual Instruments and allowed the user to set a sequence of values for the output flow from the mass flow controllers before an experimental run. This VI was named ‘vapour-sensor-sequence-timestamped.vi’. Flow rate, relative humidity and temperature data were then saved as

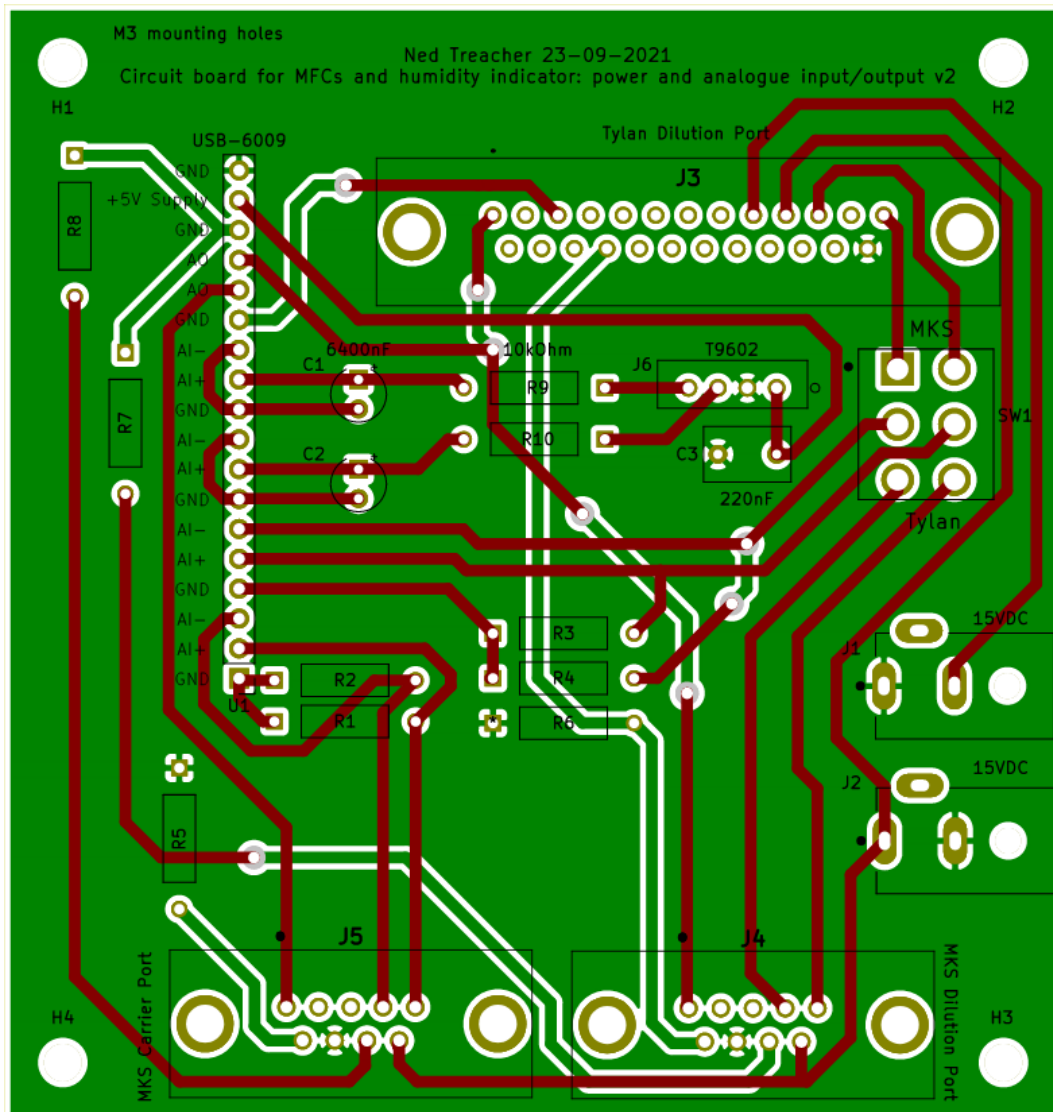


Figure 2.3.: Circuit board schematic for controlling and monitoring both the mass flow controllers and the relative humidity and temperature sensor. Resistors R1-R6 are all 10 kOhm, while R7-R8 are both 0 Ohm. The circuit board was designed using the KiCad Layout Editor.

.lvm files. The LabView VIs described here are available on request.

## 2.3. Design

### 2.3.1. Initial Design

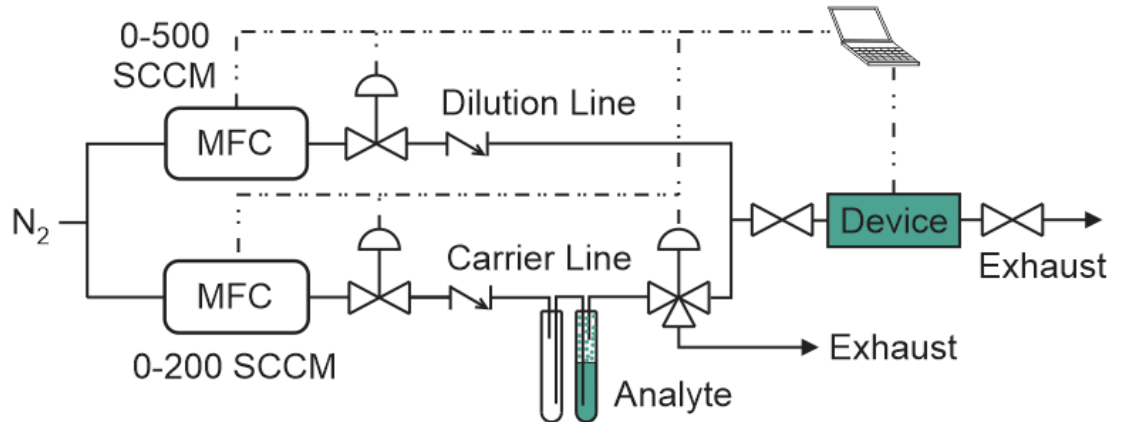


Figure 2.4.: P&ID of the original vapour delivery system

The initial design of the vapour delivery system, as shown in Figure 2.4, was relatively simple. No reference sensors were included in the setup, and only one channel could be characterised without opening the chamber and changing the position of the device. However, as constructed it worked well as a self-contained system, which was able to deliver vapour to a device channel while measuring current across the channel. A 500 sccm full-range MFC (Tylan) was placed on the dilution line, and a 200 sccm full-range MFC (Tylan) was placed on the carrier line. A glass container for analyte was present on the carrier line, with a vapour trap upstream to collect any backflow. The vapour trap was removed in later iterations due to the presence of a check valve to prevent backflow. The device chamber and mass flow controllers were connected to a laptop and an Agilent 4156C semiconductor parameter analyser and controlled using LabView.

### 2.3.2. Stage I Design

The first stage of the vapour delivery system redesign, as shown in Figure 2.5, was implemented in Nov 2021. This system introduced the ability to use a 20 sccm full-range MFC (MKS Instruments) for carrier line flow and a 200 sccm full-range MFC (MKS Instruments) for either carrier or dilution line flow, to give better control when using low flow rates. The reference sensors were also implemented, with each sensor connected in parallel to the chamber exhaust. Through testing the system with ethanol

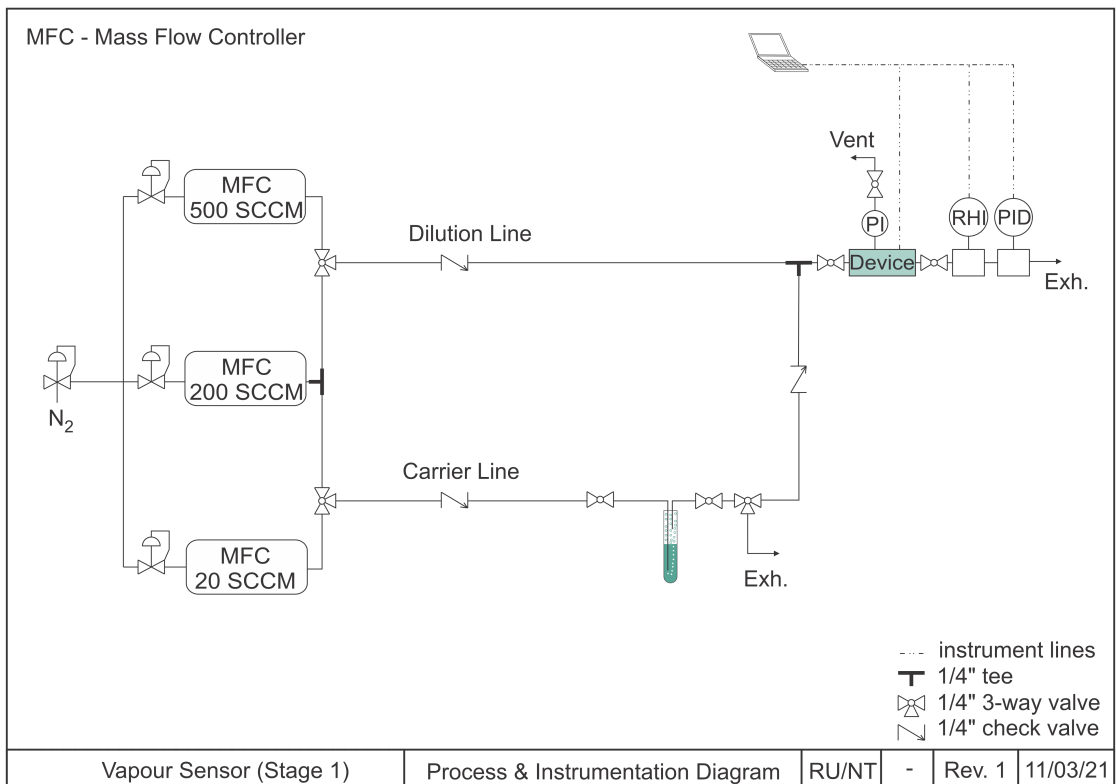


Figure 2.5.: P&ID of the Stage I vapour delivery system.

and acetone as analytes, the following issues with this implementation of the setup were identified:

- With the system connected to the lab supply of nitrogen, pressure changes in the line due to nitrogen use elsewhere in the lab impacted the pressure at the MFCs and the flow through the lines.
- The pressure indicator used for the device chamber had a much wider range than the pressure reached before nitrogen began to leak out of the PVC tubing; this meant pressure changes in the chamber, resulting from closing the exit valves while nitrogen flow entered the chamber, did not register on the indicator.
- The PID responded unexpectedly slowly to changes in vapour concentration in the chamber. For example, after acetone or ethanol vapour had been run through the chamber, running clean nitrogen through the system for 3 hours was required before the PID returned to a constant baseline reading.
- There was no way to ensure the device chamber was free of analyte vapour before an experimental run aside from running nitrogen through the dilution line. After prolonged use, condensed analyte was sometimes visible in the PVC lines of the delivery system.

These issues, along with various minor structural and design issues, were addressed in the second-stage implementation of the system.

### 2.3.3. Stage II Design

Figure 2.6 gives an overview of the second-stage design for the vapour delivery system setup. This stage of the redesign was implemented between Jan and May 2022. Changes from the first stage included:

- The addition of a N<sub>2</sub> cylinder (152D size) as the source of nitrogen for the system to replace the lab supply.
- A pressure indicator with a lower pressure range was used, which could register pressure changes within the device chamber.
- A chamber manifold was placed before the exhaust with outlets into the PID and RHI.
- A micro diaphragm pump was introduced between the manifold and PID to supply the PID with vapour from the chamber, and a flowmeter was placed before the pump to measure the flow rate out of the chamber to the PID. The PID was then seen to respond quickly to system changes (discussed further in Section 2.4).
- A piece of PVC tubing was placed at the PID outlet to limit air from the fumehood entering the PID when the micropump was off.

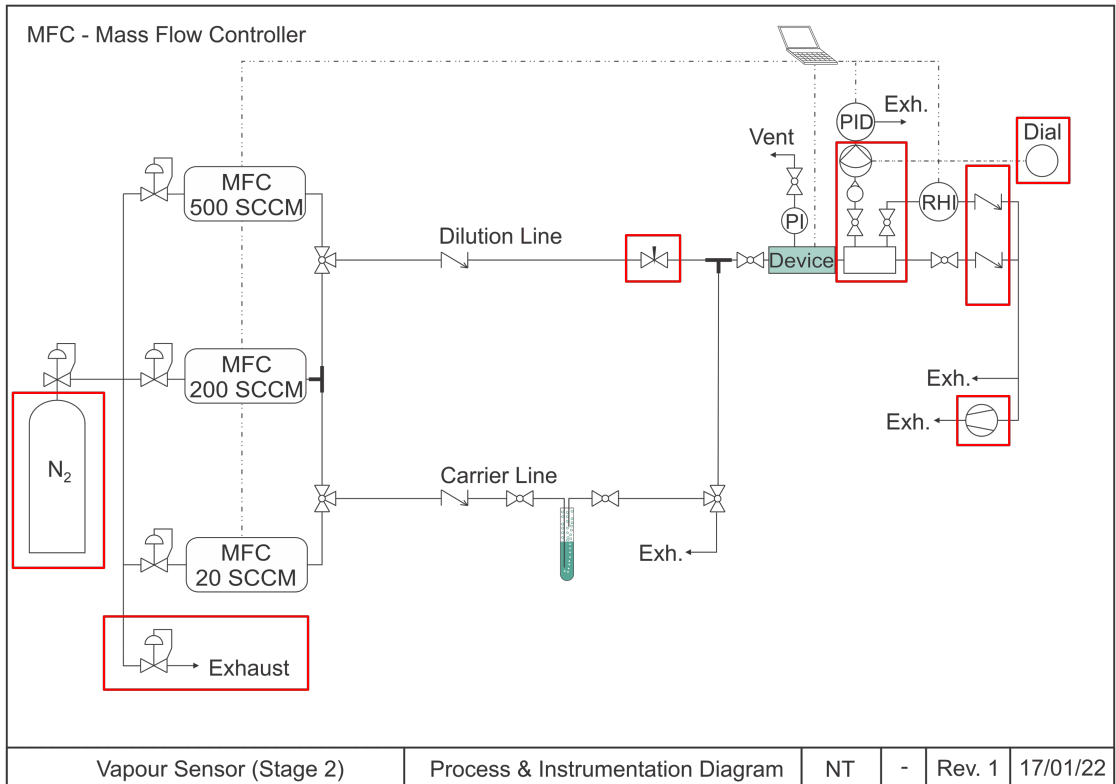


Figure 2.6.: Process & instrumentation diagram (P&ID) of the second-stage design for the vapour delivery system. Red outlines indicate additions introduced to the system subsequent to the first stage design.

- Valves were placed before all system components so that the device chamber and post-analyte bottle carrier line could be evacuated with a roughing pump without potentially affecting components.
- Check valves were placed at the exhaust to prevent backflow from the roughing pump into the delivery system.

These changes largely addressed the issues identified in Section 2.3.2.

## 2.4. Calibration and Measurements of Vapour Flow

### 2.4.1. Chamber Flow Calibration

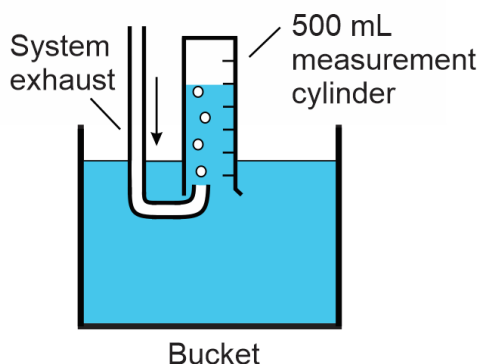


Figure 2.7.: Setup for calibration of mass flow controllers using the water displacement method.

A water displacement test was carried out to determine the relationship between the flow rate measured by the mass flow controllers and the actual flow rate passing through the chamber. All valves were set so that both the dilution and carrier lines followed a single path. Both these paths went through the device chamber and out through the system exhaust. An empty analyte bottle was placed on the carrier line. The system exhaust was placed into a bucket filled with tap water, with the outlet sitting beneath an upturned 500 mL measurement cylinder, as pictured in Figure 2.7. The cylinder was used to measure the volume of displaced water over time, which is equivalent to the rate of change of nitrogen volume entering the cylinder from the exhaust. Measurements were taken from the bottom of the meniscus of the water in the cylinder. As leaks from the manifold, chamber and exhaust line were not detected when leak testing with bubble solution, it can be safely assumed that the rate at which nitrogen exits the exhaust is equivalent to the nitrogen flow rate through the device chamber.

The time taken to displace 50 mL of water was measured three times for a series of constant flow rates, both for the 200 sccm MFC (MKS) on the carrier line and the 500

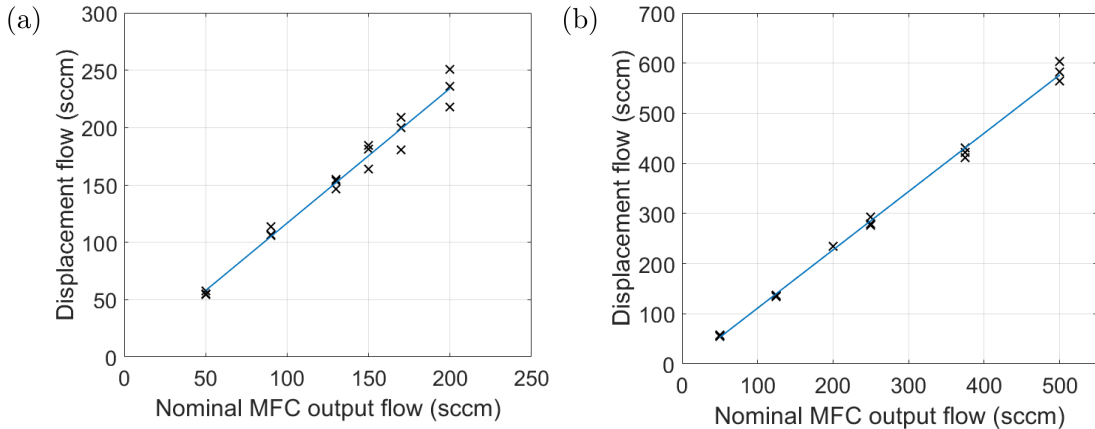


Figure 2.8.: The nominal flow rate as measured by the mass flow controller compared to the actual flow rate measured using water displacement testing, shown for the 200 sccm full-scale mas flow controller placed through the carrier line in (a), and for the 500 sccm full-scale mass flow controller placed through the dilution line in (b). Three water displacement tests were performed for each constant flow rate.

sccm MFC (Tylan) on the dilution line. The displacement flow rate corresponding to each measurement could then be found by dividing volume by time. These measurements, of displacement flow relative to nominal flow through the MFC, are shown in Figure 2.8 (a) and (b) respectively. The increased uncertainty for higher flow measurements is largely due to rapid flows being more difficult to measure precisely. However, increased instability of flow at higher flow rates may also contribute. A strong linear relationship between the nominal flow reading and actual flow was identified. A linear least-squares fit with 95% confidence interval was performed, where coefficients  $a_1$  and  $a_2$  were found for the linear relationship  $D = a_1 d + a_2$ . Here,  $d$  is nominal flow from the MFC and  $D$  is measured displacement flow. For the 200 sccm MFC flow through the carrier line, values of  $a_1 = 1.18 \pm 0.09$  and  $a_2 = -1 \pm 13$  were obtained, while for the 500 sccm MFC flow through the dilution line, values of  $a_1 = 1.16 \pm 0.04$  and  $a_2 = -5 \pm 10$  were obtained.

It appears that the offset between the measured displacement flow and nominal output flow is not due to leaks in the system, since the offset indicates measured flow exceeds the nominal flow. Instead, the offset appears to be a systematic error introduced by the electronics or software used to record the output flow from the MFCs. The identical offset between measured and nominal flow observed for each MFC, even when placed on different lines to the chamber, further strengthens the likelihood of the offset being due to the control side of the system. Furthermore, as both the carrier and dilution MFCs show readings with the same offset multiplier within a 95% confidence interval, the same offset should apply to a mixture of flows on each line. For example, a 200 sccm nominal flow through the dilution line from the 500 sccm full-scale MFC should have a roughly identical actual flow rate to a 50 sccm nominal flow through the dilution line

and a 150 sccm flow through the carrier line. In this work, tests performed with the vapour delivery system have flow rate stated in terms of their nominal value. However, the reader should keep in mind the  $1.16 - 1.18 \times$  offset between the nominal and actual chamber flow.

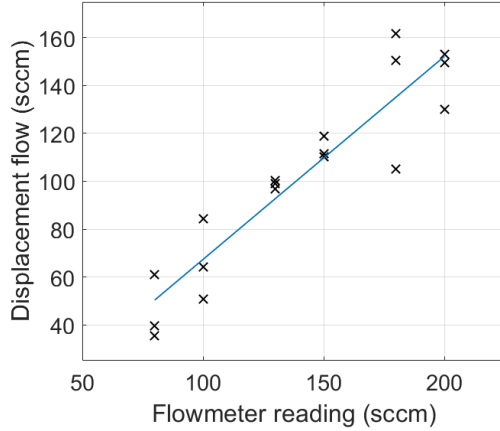


Figure 2.9.: Comparison of flowmeter readings with flow measurements from water displacement testing. Three water displacement tests were performed for each constant flow rate.

The time taken to displace a fixed water volume was also measured three times for a series of constant flow rates through the flowmeter from the chamber to exhaust. A least-squares linear relationship was obtained between flowmeter readings and actual displacement, as shown in Figure 2.9. Expressing the relationship as  $D = b_1 f + b_2$ , where  $f$  is the flowmeter reading and  $D$  is measured displacement flow, values of  $b_1 = 0.85 \pm 0.2$  and  $b_2 = -18 \pm 26$  were obtained. The flow as read from the flowmeter became less stable for flows above 150 sccm and below 130 sccm, increasing measurement uncertainty. To understand the cause of this instability, flow through the chamber was placed directly through the flowmeter without the micropump present. Relatively stable measurements could then be achieved, indicating that the flow rate instability results from the micropump used for vapour delivery when used outside the 130 – 150 sccm range. The micropump flow measured as 150 sccm on the flowmeter was generally used when measuring vapour flow through the delivery system to the photoionisation detector. Figure 2.9 indicates 150 sccm on the flowmeter corresponds to  $\sim 110$  sccm of actual flow.

#### 2.4.2. Sensor Responses to Vapour Flow

Once the rate of flow through the device chamber had been calibrated, the correct operation of the reference sensors used in the system was verified. Various flow rates in and out of the chamber were used to calibrate and verify the reference sensors. These flows in and out of the chamber are labelled on the simplified schematic in Figure 2.10.

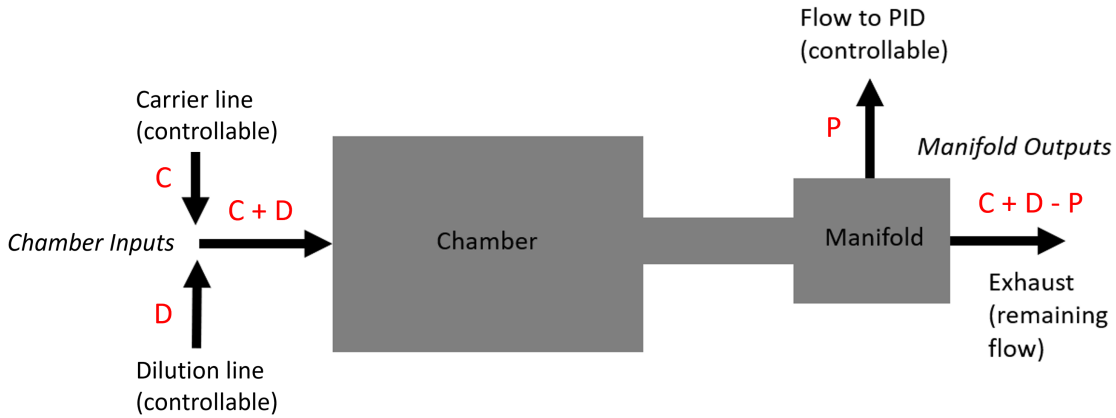


Figure 2.10.: Simplified schematic showing the flow into and out of the device chamber and manifold of the delivery system. The input flows from the carrier and dilution line are represented by C and D, and the output flow through the PID is represented by P. The exhaust can either flow past the relative humidity indicator or straight to the fumehood. This diagram assumes that flow through leaks in the chamber and manifold is low enough to be considered negligible, which was confirmed by leak testing with bubble solution.

Note that the labels on this schematic assume that nitrogen compression at any point within this schematic is negligible. Section 2.4.1 shows that a 200 sccm flow into the chamber corresponds to an actual rate for  $C + D$  of  $\sim 230$  sccm. If a 150 sccm flow rate as measured by the flowmeter is pumped out through the PID, Section 2.4.1 shows that  $P \sim 110$  sccm. This means that  $\sim 50\%$  of the flow through the chamber exits via the PID. If a 100 sccm flowmeter rate is pumped through the PID,  $P \sim 70$  sccm, and therefore  $\sim 30\%$  of the chamber flow exits through the PID.

### Relative Humidity Indicator

Table 2.1.: Flow sequence for testing relative humidity indicator.

t (s)	C (sccm)	D (sccm)
200	0	400
200	100	300
200	200	200
200	200	100
200	200	0

To test the relative humidity indicator (RHI), all valves out of the chamber were sealed

except for the valve for the relative humidity indicator chamber. This meant all flow coming out of the system would pass through the relative humidity indicator chamber ( $P = 0$  sccm and exhaust goes to RHI in Figure 2.10). Continuous nitrogen flow was then placed through the chamber until relative humidity dropped to about 20%. 10 mL of deionised water was placed into the analyte bottle. A series of different flow rates through each line was sent to the chamber, with the sequence of flow rates shown in Table 2.1 ( $t$  = time,  $C$  = carrier line flow rate,  $D$  = dilution line flow rate). Note that between 200 s and 600 s, the total flow rate remains the same, but the ratio of dilution to carrier flow differs.

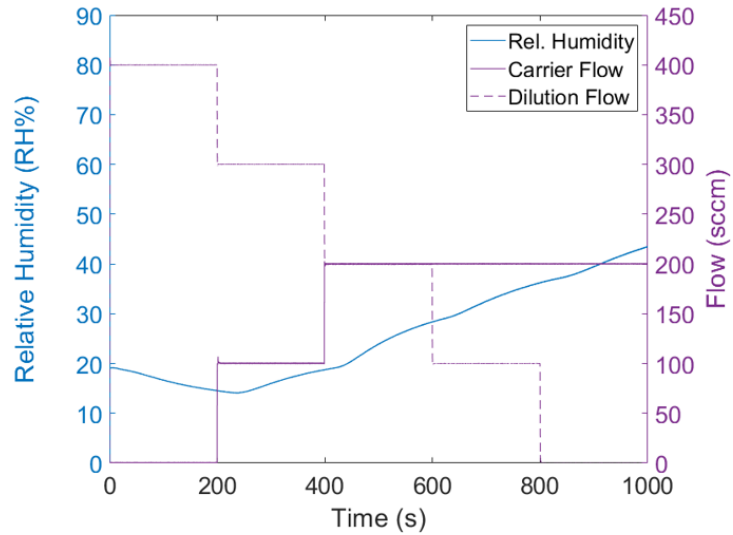


Figure 2.11.: Relative humidity readouts from the relative humidity indicator juxtaposed with flow rates from the dilution line and carrier lines of the vapour system, with 10 mL deionised water in the carrier line analyte bottle.

Figure 2.11 shows that the Telaire sensor records decreased humidity after flow exclusively from the dilution line and increased humidity after flow from the analyte bottle. It also shows that in regular 200 s intervals, the rate of relative humidity change increases and then begins to stabilise. Each accelerated change in relative humidity occurs about 50 s after a corresponding increase in flow through the carrier line. It appears a 50 s period passes before an increased concentration of water vapour due to increased carrier flow first reaches the relative humidity indicator. Over the full 800 s of carrier line flow, relative humidity increases from a minimum of  $14.0 \pm 2.0\%$  to a maximum of  $43.6 \pm 2.0\%$ . The temperature in the chamber remained between  $21.0 \pm 0.5^\circ\text{C}$  and  $22.0 \pm 0.5^\circ\text{C}$  over the entire measurement period. Combining equations Equation 2.1 and Equation 2.2 from Section 2.2.2, we find that the absolute humidity in the chamber reaches a low of  $2.6 \pm 0.4 \text{ gm}^{-3}$  at 238.1 s, 38.1 s after the initial onset of carrier flow, and a high of  $8.4 \pm 0.5 \text{ gm}^{-3}$  at 998.8 s, after 798.8 s of carrier flow through the chamber. The clear response of the Telaire RHI to increased water vapour flow confirms that this sensor is working.

## **Photoionisation Detector with Continuous Vapour Flow**

To test the photoionisation detector, the device chamber and carrier line were first purged of vapour through the exhaust using a roughing pump, with the PID valve closed to protect it from the pump. The PID valve was then opened, the micropump was set to 150 sccm as read by the flowmeter. During testing with the PID, the total flow into the chamber was set at 200 sccm as read by the Tylan mass flow controllers. The calibration curves in Section 2.4.1 show that the actual flow C + D was then therefore approximately the same as the actual flow rate into the PID, P. A flow of 200 sccm nitrogen was placed through the dilution line to the chamber for 10 minutes until successive concentration readings from the PID were either approximately constant, or until baseline drift was small enough to be considered negligible. These measurements were then used as the baseline (0 ppm) for subsequent measurements. 5 mL of the volatile organic compound ethyl hexanoate (EtHex), also known as ethyl caproate, was placed into the analyte bottle. A flow of 150 sccm was then sent through the carrier line and 50 sccm through the dilution line for 600 s. The same procedure was performed on two separate dates spaced three days apart (23 Feb and 26 Feb) to check that the measured PID response to ethyl hexanoate vapour pumped out of the manifold was repeatable.

The responses from each date are shown in Figure 2.12. In Figure 2.12 (a), the response corresponding to each measurement date is shown unnormalised, with the parts per million concentration shown relative to the nitrogen baseline as recorded by the PID. Both measurements show little to no response to vapour for approximately 50 s, which seems to be the time taken for vapour to first reach the PID. Over the next 100s, there is a rapid increase in vapour concentration detected, which then settles to a constant concentration at about 300 s. This appears to be the maximum concentration of EtHex vapour that can be contained by the chamber in this configuration. There is approximately a 200 parts per billion difference in maximum concentration between the measurement on each date.

However, this is not unexpected. As discussed in Section 2.2.2, the PID is being run uncalibrated, and some drift of the sensitivity of the sensor due to environmental changes is highly likely. To check that the PID records the same evolution of vapour flow with time, regardless of its sensitivity, the measurements from both dates were then normalised with respect to the maximum concentration reading. Figure 2.12 (b) shows that once normalised, the rate of change in concentration with time is almost identical between the two measurement sets. This test verifies that the evolution of vapour concentration of the device chamber can be repeatably measured using the PID in the vapour delivery system.

## **Photoionisation Detector with Vapour Flow Intervals**

A further series of tests were performed to verify whether it was possible to compare different concentrations of vapour in the chamber using the PID. All testing was performed

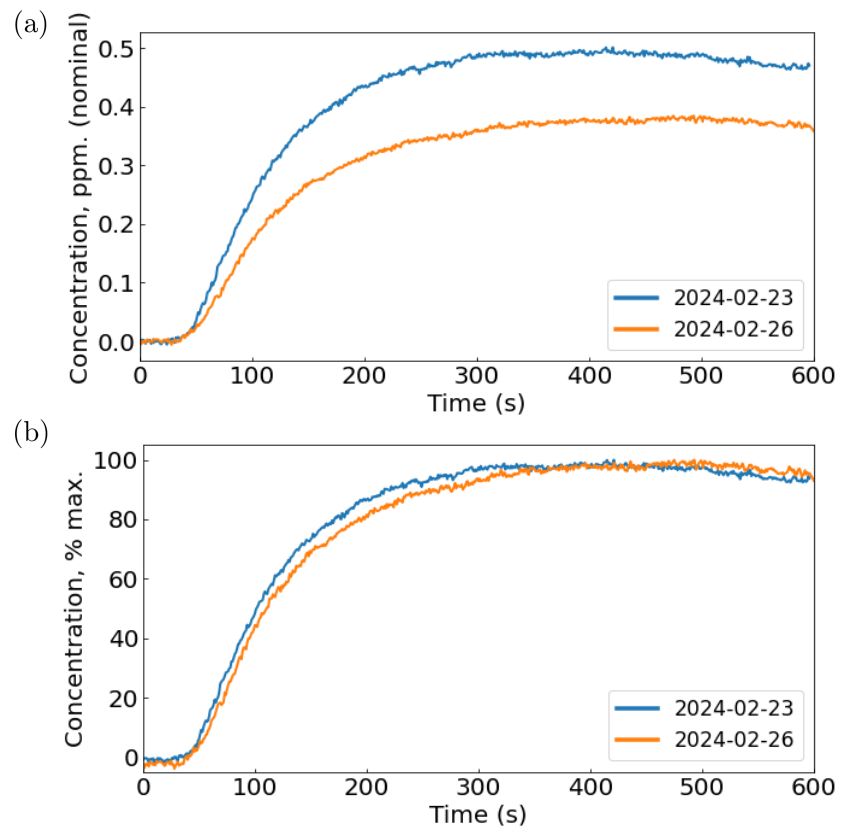


Figure 2.12.: The response of the photoionisation detector to ethyl hexanoate vapour over 600 s of exposure is shown relative to the 200 sccm nitrogen flow baseline in (a), and normalised with respect to the maximum reading in (b).

on the same day to minimise sensitivity drift. For each test, the system was purged of vapour and the total dilution flow into the chamber was set at 200 sccm as read by the Tylan mass flow controller. Flow out of the chamber to the PID was set at 100 sccm as read by the micropump flowmeter, and the almost-constant nitrogen baseline after 10 minutes was set as the PID zero point. 5 mL of the volatile organic compound ethyl hexanoate (EtHex) was placed into the analyte bottle. During each test, 200 sccm was continuously flowed through the dilution line, except during three evenly spaced intervals of equal length. During these intervals, 150 sccm flow was placed through the carrier line and 50 sccm flow placed through the dilution line. In each test, the input interval time was varied to examine its effect on maximum vapour concentration recorded by the PID. As it took longer for the PID to return to a constant baseline with increased input intervals, when the input interval was increased, the spacing between intervals was also increased.

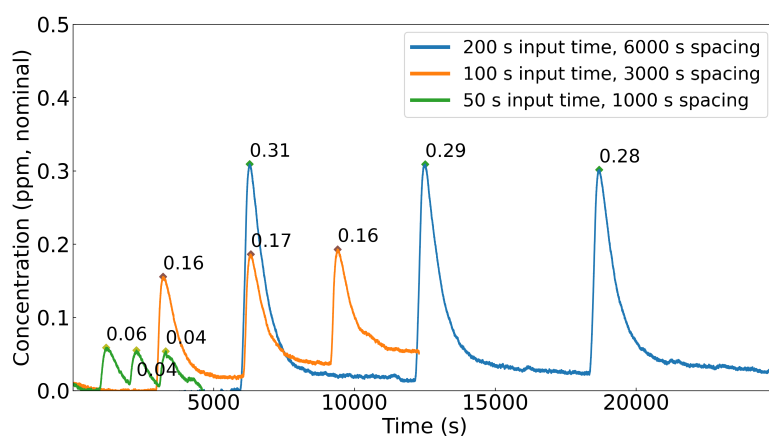


Figure 2.13.: The response of the photoionisation detector to 3 evenly-spaced intervals of ethyl hexanoate vapour entering the device chamber, relative to a 200 sccm nitrogen flow baseline. Input intervals were either either 50 s, 100 s or 200 s in length. During each input interval, 150 sccm carrier flow and 50 sccm dilution flow was placed through the chamber.

The results of three tests, with input intervals of 50 s, 100 s and 200 s, are shown in Figure 2.13. Each interval of carrier flow corresponds to a rapid increase in concentration, which reaches a peak, then decreases. The maximum concentration reached for each interval is shown above the corresponding peak. Note that the maximum concentration label does not correspond to the difference between the original baseline and the maximum concentration of each peak. Instead, it corresponds to the difference between the concentration measurement at a set time before the onset of carrier flow and the maximum concentration reached. For each test, this set time is 5% of the spacing time used, 50 s, 150 s and 300 s respectively. This approach was taken to account for what appears to be drift from the original 0 ppm baseline. This variable baseline drift was particularly significant for the 100 s interval measurements, where concentration

measurements settled to a new baseline of  $\sim 0.05$  ppm after the third peak.

The values of three concentration maxima in each test are highly consistent, with only a  $\pm 0.02$  ppm margin of error. This experiment demonstrates that if tests using the PID are performed during the same day, placing the same vapour flow into the PID for the same interval of time in each test, it is possible to measure the same maximum concentration with the PID. It furthermore indicates that the placing the same amount of vapour flow into the chamber for a set amount of time leads to a reproducible concentration of vapour building up within the chamber. Drift in the baseline does not significantly affect the magnitude of each concentration peak when measured relative to the baseline reading directly before each interval.

## 2.5. Summary

A custom vapour delivery system was made suitable for field-effect biosensor work through ensuring a range of flows could be delivered through the system and that reference sensors were available for corroboration with the readings on the field-effect biosensors. Two new mass flow controllers with different maximum flow rates and two reference sensors, a relative humidity and temperature sensor and photoionisation detector, were introduced to the system in a two-stage design process. A new electronic control system and LabView software were designed and constructed for the altered delivery system. The nitrogen flow through the system was then calibrated using water displacement testing, and it was verified that the reference sensors both worked as expected.

# References

- [1] Sang Hun Lee and Tai Hyun Park. "Recent advances in the development of bio-electronic nose". In: *Biotechnology and Bioprocess Engineering* 15.1 (Feb. 2010), pp. 22–29. ISSN: 12268372. DOI: 10.1007/S12257-009-3077-1/METRICS. URL: <https://link.springer.com/article/10.1007/s12257-009-3077-1>.
- [2] Tran Thi Dung, Yunkwang Oh, Seon Jin Choi, et al. "Applications and Advances in Bioelectronic Noses for Odour Sensing". In: *Sensors 2018, Vol. 18, Page 103* 18.1 (Jan. 2018), p. 103. ISSN: 1424-8220. DOI: 10.3390/S18010103. URL: <https://www.mdpi.com/1424-8220/18/1/103>.
- [3] Dongseok Moon, Yeon Kyung Cha, So ong Kim, et al. "FET-based nanobiosensors for the detection of smell and taste". In: *Science China. Life sciences* 63.8 (Aug. 2020), pp. 1159–1167. ISSN: 1869-1889. DOI: 10.1007/S11427-019-1571-8. URL: <https://pubmed.ncbi.nlm.nih.gov/31974862/>.
- [4] Bajramshahe Shkodra, Mattia Petrelli, Martina Aurora Costa Angeli, et al. "Electrolyte-gated carbon nanotube field-effect transistor-based biosensors: Principles and applications". In: *Applied Physics Reviews* 8.4 (Dec. 2021), p. 41325. ISSN: 19319401. DOI: 10.1063/5.0058591. URL: [/aip/apr/article/8/4/041325/1076095/Electrolyte-gated-carbon-nanotube-field-effect](https://aip.org/aim/article/8/4/041325/1076095/Electrolyte-gated-carbon-nanotube-field-effect).
- [5] Thanihaichelvan Murugathas, Han Yue Zheng, Damon Colbert, et al. "Biosensing with Insect Odorant Receptor Nanodiscs and Carbon Nanotube Field-Effect Transistors". In: *ACS Applied Materials and Interfaces* 11.9 (Mar. 2019), pp. 9530–9538. ISSN: 19448252. DOI: 10.1021/ACSAM.8B19433. URL: <https://pubs.acs.org/doi/full/10.1021/acsami.8b19433>.
- [6] Thanihaichelvan Murugathas, Cyril Hamiaux, Damon Colbert, et al. "Evaluating insect odorant receptor display formats for biosensing using graphene field effect transistors". In: *ACS Applied Electronic Materials* 2.11 (Nov. 2020), pp. 3610–3617. ISSN: 26376113. DOI: 10.1021/ACSAELM.0C00677. URL: <https://pubs.acs.org/doi/full/10.1021/acsaelm.0c00677>.
- [7] Daigo Terutsuki, Hidefumi Mitsuno, Kohei Sato, et al. "Highly effective volatile organic compound dissolving strategy based on mist atomization for odorant biosensors". In: *Analytica Chimica Acta* 1139 (Dec. 2020), pp. 178–188. ISSN: 0003-2670. DOI: 10.1016/J.ACA.2020.09.043.

- [8] Takahiro Arakawa, Takuma Suzuki, Masato Tsujii, et al. “Real-time monitoring of skin ethanol gas by a high-sensitivity gas phase biosensor (bio-sniffer) for the non-invasive evaluation of volatile blood compounds”. In: *Biosensors and Bioelectronics* 129 (Mar. 2019), pp. 245–253. ISSN: 0956-5663. DOI: 10.1016/J.BIOS.2018.09.070.
- [9] Heehong Yang, Daesan Kim, Jeongsu Kim, et al. “Nanodisc-Based Bioelectronic Nose Using Olfactory Receptor Produced in Escherichia coli for the Assessment of the Death-Associated Odor Cadaverine”. In: *ACS Nano* 11.12 (Dec. 2017), pp. 11847–11855. ISSN: 1936086X. DOI: 10.1021/ACSNANO.7B04992/ASSET/IMAGES/NN-2017-04992T\_M003.GIF. URL: <https://pubs.acs.org/doi/full/10.1021/acsnano.7b04992>.
- [10] Manki Son, Daesan Kim, Hwi Jin Ko, et al. “A portable and multiplexed bioelectronic sensor using human olfactory and taste receptors”. In: 87 (Jan. 2017), pp. 901–907. DOI: 10.1016/J.BIOS.2016.09.040. URL: <https://pubmed.ncbi.nlm.nih.gov/27664409/>.
- [11] Ariella Y. Moser, Wendy Y. Brown, Lewis A. Bizo, et al. “Biosecurity Dogs Detect Live Insects after Training with Odor-Proxy Training Aids: Scent Extract and Dead Specimens”. In: *Chemical Senses* 45.3 (Apr. 2020), pp. 179–186. ISSN: 14643553. DOI: 10.1093/CHEMSE/BJAA001. URL: <https://dx.doi.org/10.1093/chemse/bjaa001>.
- [12] Roshan Khadka, Nihan Aydemir, Colm Carraher, et al. “An ultrasensitive electrochemical impedance-based biosensor using insect odorant receptors to detect odorants”. In: *Biosensors and Bioelectronics* 126 (Feb. 2019), pp. 207–213. ISSN: 0956-5663. DOI: 10.1016/J.BIOS.2018.10.043.
- [13] “piD-TECH® eVx User Manual 143-175 Rev 1.0”. URL: <https://www.ametekmocon.com/products/oemphotoionization/pidtechevxphotoionizationdetector>.
- [14] *Technical Application Articles - Ion Science UK*. URL: <https://ionscience.com/en/gas-and-leak-detectors/customer-support/documents/technical-application-articles/> (visited on 2024-02-27).
- [15] Amphenol Advanced Sensors. *Telaire T9602 Humidity and Temperature Sensor*. URL: <https://www.amphenol-sensors.com/en/telaire/humidity/527-humidity-sensors/3224-t9602> (visited on 2024-02-26).
- [16] *The Capacitive Humidity Sensor*. URL: [https://www.rotronic.com/en/humidity-measurement-feuchtemessung-mesure\\_de\\_1\\_humidite/capacitive-sensors-technical-notes-mr](https://www.rotronic.com/en/humidity-measurement-feuchtemessung-mesure_de_1_humidite/capacitive-sensors-technical-notes-mr) (visited on 2024-02-26).
- [17] *Make Your Job Easier with Humidity Conversion Formulas / Vaisala*. URL: <https://www.vaisala.com/en/lp/make-your-job-easier-humidity-conversion-formulas> (visited on 2024-02-26).

## A. Vapour System Hardware

Table A.1.: Major components used in construction of the vapour delivery system described in this thesis.

Description	Part No.	Manufacturer
Mass flow controller, 20 sccm full scale	GE50A-013201SBV020	MKS Instruments
Mass flow controller, 200 sccm full scale	GE50A-013202SBV020	MKS Instruments
Mass flow controller, 500 sccm full scale	FC-2901V	Tylan
Analogue flowmeter, 240 sccm max. flow	116261-30	Dwyer
Micro diaphragm pump	P200-B3C5V-35000	Xavitech
Analogue flow controller, for micro diaphragm pump	X3000450	Xavitech
10 mL Schott bottle	218010802	Duran
PTFE connection cap system	Z742273	Duran
Baseline VOC-TRAQ flow cell, purple	043-950	Ametek Mocon
Baseline VOC-TRAQ flow cell, red	043-951	Ametek Mocon
Humidity and temperature sensor	T9602-5-A	Telaire
Enclosure, for humidity and temperature sensor	MC001189	Multicomp Pro



## B. Python Code for Data Analysis

### B.1. Code Repository

The code used for general analysis of field-effect transistor devices in this thesis was written with Python 3.8.8. Contributors to the code used include Erica Cassie, Erica Happe, Marissa Dierkes and Leo Browning. The code is located on GitHub and the research group OneDrive, and is available on request.

### B.2. Atomic Force Microscope Histogram Analysis

The purpose of this code is to analyse atomic force microscope (AFM) images of carbon nanotube networks in .xyz format taken using an atomic force microscope and processed in Gwyddion (see [?@sec-afm-characterisation](#)). It was originally designed by Erica Happe in Matlab, and adapted by Marissa Dierkes and myself for use in Python. The code imports the .xyz data and sorts it into bins 0.15 nm in size for processing. To perform skew-normal distribution fits, both *scipy.optimize.curve\_fit* and *scipy.stats.skewnorm* modules are used in this code.

### B.3. Raman Spectroscopy Analysis

The purpose of this code is to analyse a series of Raman spectra taken at different points on a single film (see [?@sec-raman-characterisation](#)). Data is imported in a series of tab-delimited text files, with the low wavenumber spectrum ( $100\text{ cm}^{-1} - 650\text{ cm}^{-1}$ ) and high wavenumber spectrum ( $1300\text{ cm}^{-1} - 1650\text{ cm}^{-1}$ ) imported in separate datafiles for each scan location.

### B.4. Field-Effect Transistor Analysis

The purpose of this code is to analyse electrical measurements taken of field-effect transistor (FET) devices. Electrical measurements were either taken from the Keysight 4156C Semiconductor Parameter Analyser, National Instruments NI-PXIe or Keysight B1500A Semiconductor Device Analyser as discussed in [?@sec-electrical-characterisation](#);

the code is able to analyse data in .csv format taken from all three measurement setups. The main Python file in the code base consists of three related but independent modules: the first analyses and plots sensing data from the FET devices, the second analyses and plots transfer characteristics from channels across a device, and the third compares individual channel characteristics before and after a modification or after each of several modifications. The code base also features a separate config file and style sheet which govern the behaviour of the main code. The code base was designed collaboratively by myself and Erica Cassie over GitHub using the Sourcetree Git GUI.

# References

- [1] Sang Hun Lee and Tai Hyun Park. "Recent advances in the development of bio-electronic nose". In: *Biotechnology and Bioprocess Engineering* 15.1 (Feb. 2010), pp. 22–29. ISSN: 12268372. DOI: 10.1007/S12257-009-3077-1/METRICS. URL: <https://link.springer.com/article/10.1007/s12257-009-3077-1>.
- [2] Tran Thi Dung, Yunkwang Oh, Seon Jin Choi, et al. "Applications and Advances in Bioelectronic Noses for Odour Sensing". In: *Sensors 2018, Vol. 18, Page 103* 18.1 (Jan. 2018), p. 103. ISSN: 1424-8220. DOI: 10.3390/S18010103. URL: <https://www.mdpi.com/1424-8220/18/1/103>.
- [3] Dongseok Moon, Yeon Kyung Cha, So ong Kim, et al. "FET-based nanobiosensors for the detection of smell and taste". In: *Science China. Life sciences* 63.8 (Aug. 2020), pp. 1159–1167. ISSN: 1869-1889. DOI: 10.1007/S11427-019-1571-8. URL: <https://pubmed.ncbi.nlm.nih.gov/31974862/>.
- [4] Bajramshahe Shkodra, Mattia Petrelli, Martina Aurora Costa Angeli, et al. "Electrolyte-gated carbon nanotube field-effect transistor-based biosensors: Principles and applications". In: *Applied Physics Reviews* 8.4 (Dec. 2021), p. 41325. ISSN: 19319401. DOI: 10.1063/5.0058591. URL: [/aip/apr/article/8/4/041325/1076095/Electrolyte-gated-carbon-nanotube-field-effect](https://aip.org/aim/article/8/4/041325/1076095/Electrolyte-gated-carbon-nanotube-field-effect).
- [5] Thanihaichelvan Murugathas, Han Yue Zheng, Damon Colbert, et al. "Biosensing with Insect Odorant Receptor Nanodiscs and Carbon Nanotube Field-Effect Transistors". In: *ACS Applied Materials and Interfaces* 11.9 (Mar. 2019), pp. 9530–9538. ISSN: 19448252. DOI: 10.1021/ACSAM.8B19433. URL: <https://pubs.acs.org/doi/full/10.1021/acsami.8b19433>.
- [6] Thanihaichelvan Murugathas, Cyril Hamiaux, Damon Colbert, et al. "Evaluating insect odorant receptor display formats for biosensing using graphene field effect transistors". In: *ACS Applied Electronic Materials* 2.11 (Nov. 2020), pp. 3610–3617. ISSN: 26376113. DOI: 10.1021/ACSAELM.0C00677. URL: <https://pubs.acs.org/doi/full/10.1021/acsaelm.0c00677>.
- [7] Daigo Terutsuki, Hidefumi Mitsuno, Kohei Sato, et al. "Highly effective volatile organic compound dissolving strategy based on mist atomization for odorant biosensors". In: *Analytica Chimica Acta* 1139 (Dec. 2020), pp. 178–188. ISSN: 0003-2670. DOI: 10.1016/J.ACA.2020.09.043.

- [8] Takahiro Arakawa, Takuma Suzuki, Masato Tsujii, et al. “Real-time monitoring of skin ethanol gas by a high-sensitivity gas phase biosensor (bio-sniffer) for the non-invasive evaluation of volatile blood compounds”. In: *Biosensors and Bioelectronics* 129 (Mar. 2019), pp. 245–253. ISSN: 0956-5663. DOI: 10.1016/J.BIOS.2018.09.070.
- [9] Heehong Yang, Daesan Kim, Jeongsu Kim, et al. “Nanodisc-Based Bioelectronic Nose Using Olfactory Receptor Produced in Escherichia coli for the Assessment of the Death-Associated Odor Cadaverine”. In: *ACS Nano* 11.12 (Dec. 2017), pp. 11847–11855. ISSN: 1936086X. DOI: 10.1021/ACSNANO.7B04992/ASSET/IMAGES/NN-2017-04992T\_M003.GIF. URL: <https://pubs.acs.org/doi/full/10.1021/acsnano.7b04992>.
- [10] Manki Son, Daesan Kim, Hwi Jin Ko, et al. “A portable and multiplexed bioelectronic sensor using human olfactory and taste receptors”. In: 87 (Jan. 2017), pp. 901–907. DOI: 10.1016/J.BIOS.2016.09.040. URL: <https://pubmed.ncbi.nlm.nih.gov/27664409/>.
- [11] Ariella Y. Moser, Wendy Y. Brown, Lewis A. Bizo, et al. “Biosecurity Dogs Detect Live Insects after Training with Odor-Proxy Training Aids: Scent Extract and Dead Specimens”. In: *Chemical Senses* 45.3 (Apr. 2020), pp. 179–186. ISSN: 14643553. DOI: 10.1093/CHEMSE/BJAA001. URL: <https://dx.doi.org/10.1093/chemse/bjaa001>.
- [12] Roshan Khadka, Nihan Aydemir, Colm Carraher, et al. “An ultrasensitive electrochemical impedance-based biosensor using insect odorant receptors to detect odorants”. In: *Biosensors and Bioelectronics* 126 (Feb. 2019), pp. 207–213. ISSN: 0956-5663. DOI: 10.1016/J.BIOS.2018.10.043.
- [13] “piD-TECH® eVx User Manual 143-175 Rev 1.0”. URL: <https://www.ametekmocon.com/products/oemphotoionization/pidtechevxphotoionizationdetector>.
- [14] *Technical Application Articles - Ion Science UK*. URL: <https://ionscience.com/en/gas-and-leak-detectors/customer-support/documents/technical-application-articles/> (visited on 2024-02-27).
- [15] Amphenol Advanced Sensors. *Telaire T9602 Humidity and Temperature Sensor*. URL: <https://www.amphenol-sensors.com/en/telaire/humidity/527-humidity-sensors/3224-t9602> (visited on 2024-02-26).
- [16] *The Capacitive Humidity Sensor*. URL: [https://www.rotronic.com/en/humidity-measurement-feuchtemessung-mesure\\_de\\_1\\_humidite/capacitive-sensors-technical-notes-mr](https://www.rotronic.com/en/humidity-measurement-feuchtemessung-mesure_de_1_humidite/capacitive-sensors-technical-notes-mr) (visited on 2024-02-26).
- [17] *Make Your Job Easier with Humidity Conversion Formulas / Vaisala*. URL: <https://www.vaisala.com/en/lp/make-your-job-easier-humidity-conversion-formulas> (visited on 2024-02-26).